## **Nanoscale**



**PAPER** 

View Article Online
View Journal | View Issue



Cite this: Nanoscale, 2023, 15, 12586

# Decoding the mechanical conductance switching behaviors of dipyridyl molecular junctions

Feng Sun,†<sup>a</sup> Lin Liu,†<sup>a</sup> Chang-Feng Zheng,<sup>a</sup> Yu-Chen Li,<sup>a</sup> Yan Yan,<sup>a</sup> Xiao-Xiao Fu, o a Chuan-Kui Wang,<sup>a</sup> Ran Liu, \*\overline{0}\*\* binggian Xu\*\* and Zong-Liang Li

Dipyridyl molecular junctions often show intriguing conductance switching behaviors with mechanical modulations, but the mechanisms are still not completely revealed. By applying the *ab initio*-based adiabatic simulation method, the configuration evolution and electron transport properties of dipyridyl molecular junctions in stretching and compressing processes are systematically investigated. The numerical results reveal that the dipyridyl molecular junctions tend to form specific contact configurations during formation processes. In small electrode gaps, the pyridyls almost vertically adsorb on the second Au layers of the tip electrodes by pushing the top Au atoms aside. These specific contact configurations result in stronger molecule–electrode couplings and larger electronic incident cross-sectional areas, which consequently lead to large breaking forces and high conductance. On further elongating the molecular junctions, the pyridyls shift to the top Au atoms of the tip electrodes. The additional scattering of the top Au atoms dramatically decreases the conductance and switches the molecular junctions to the lower conductive states. Perfect cyclical conductance switches are obtained as observed in the experiments by repeatedly stretching and compressing the molecular junctions. The O atom in the side-group tends to hinder the pyridyl from adsorbing on the second Au layer and further inhibits the conductance switch of the dipyridyl molecular junction.

Received 3rd February 2023, Accepted 27th June 2023 DOI: 10.1039/d3nr00505d

rsc.li/nanoscale

#### Introduction

A molecular junction refers to a system in which one or several molecules are confined between two nano-electrodes. 1-10 Due to the nanoscale dimension of the molecules and the confinement of electrodes, molecular junctions often exhibit intriguing properties which can be applied in rectifiers, 11-14 switches, 15-21 transistors, 22-24 memory devices,25-28 sensors,27-30 and logic gates.8 Therefore, in the last two decades, a great deal of attention has been paid to the design and study of molecular junctions. Generally, due to the different interactions between molecules and electrodes, molecular junctions show various electron-transport properties during their formation. Apart from using these properties to design functional devices, the properties also provide useful

Thiol, 40-45 amino 44-48 and pyridyl 49-54 groups are the most frequently used anchoring groups in molecular junctions, of which molecular junctions with pyridyl anchoring groups are the ones of most interest. This is because they tend to exhibit unique and specific high-low binary conductance switching (BCS) behaviors during their formation, whether measured in solution or in air.50-52 Different from the isomerization-transition-induced molecular switches, 19,20 the conductance switching behaviors of pyridyl-anchored molecular junctions are generally attributed to the changes of the angles between the N-Au bonds and the  $\pi$  systems with the changes of the electrode-electrode separation. 29,50,55 To further understand the high-low conductance switching (HLCS) phenomena of pyridyl-anchored molecular junctions, recently we have controlled the electromechanical switching properties of dipyridyl molecular junctions by side-group substitutions based on the scanning tunnelling microscopy-break junction (STM-BJ) technique.5 We found that the presence of alkyl side-groups switches off the mechanically controlled HLCS behaviors of dipyridyl molecular junctions and considered that the "high"

information about the formation processes of molecular junctions. Thus, by creating molecular junctions, one also establishes a platform to understand and manipulate the interactions at the single atom/molecule level. 36,39

<sup>&</sup>lt;sup>a</sup>School of Physics and Electronics, Shandong Normal University, Jinan 250358, China. E-mail: lizongliang@sdnu.edu.cn

<sup>&</sup>lt;sup>b</sup>Single Molecule Study Laboratory, College of Engineering and Nanoscale Science and Engineering Center, University of Georgia, Athens, Georgia 30602, USA. E-mail: ranliu91@gmail.com, nanoxu@uga.edu

<sup>&</sup>lt;sup>c</sup>Biodesign Center for Bioelectronics and Biosensors, School of Electrical, Computer and Energy Engineering, Arizona State University, Tempe, Arizona 85287, USA † These authors contributed equally to this work.

Nanoscale Paper

conductance geometries may be prevented by simple steric hindrance of the bulky methyl and cyclohexyl side-groups. It is obvious that changes in electrode separation tend to modulate the orientation of the molecule and further induce the conductance switch in the molecular junction. However, based on the experimental observations we find that the following significant issues are still difficult to be understood and need to be further clarified. That is, (1) how do the contact configurations of the high and low conductance states arise during the fabrication of molecular junctions? (2) How to explain the discrete conductance changes in the HLCS behaviors of molecular junctions?<sup>5,35,50</sup> (3) Why the maximal stretching forces for the high conductance states are evidently higher than the breaking forces of low conductance states for the dipyridyl molecular junction? 51,56 Considering these issues, we find that compared with the orientations of the molecules, the deformations of electrode tips are more significant for the HLCS behaviors of the dipyridyl molecular junctions. To clarify these issues and to gain a deeper insight into the HLCS behaviors of dipyridyl molecular junctions, in this work we conducted ab initio-based adiabatic stretching and compressing simulations. Based on the simulations, the configuration evolution leading to the HLCS behaviors of the dipyridyl molecular junctions is systematically revealed. In particular, the specific contact configurations between pyridyl terminals and tip Au electrodes, which are very crucial for the HLCS behaviors of dipyridyl molecular junctions, are decoded. Moreover, the force differences between high and low conductance states are perfectly reconciled, which further confirms the evolution processes. Our studies show that ab initio-based adiabatic simulations are very significant for identifying the contact configurations and decoding the evolution processes of molecular junctions.

It should be mentioned that the HLCS behavior of the 4,4′-bipyridine molecular system was investigated theoretically in our previous work.<sup>59</sup> In that work, the breaking force and the geometries of the tip electrode were ignored; thus the experimental findings could not be fully explained. Particularly, the large breaking force and the repeated HLCS behavior in the stretching and compressing processes of the molecular junction could not be reproduced. In this work, we not only consider the geometries of the tip electrode and the breaking forces of the molecular junctions, but also further investigate the effect of the side group on the HLCS behaviors of dipyridyl molecular junctions to clarify why no HLCS behavior was observed for the dipyridyl molecules with methyl and cyclohexyl side substituents.

# II. Theoretical models and computational details

The schematic structures of the dipyridyl molecular junctions which include 4,4'-bipyridine (BPY) and its derivative systems are shown in Fig. 1, where M1 is 4,4'-bipyridine. M2 is 3,3'-dibromo-4,4'-bipyridine, which has a similar structure to M1. M3 and M4 are two phosphoryl-bridged dipyridyls with methyl

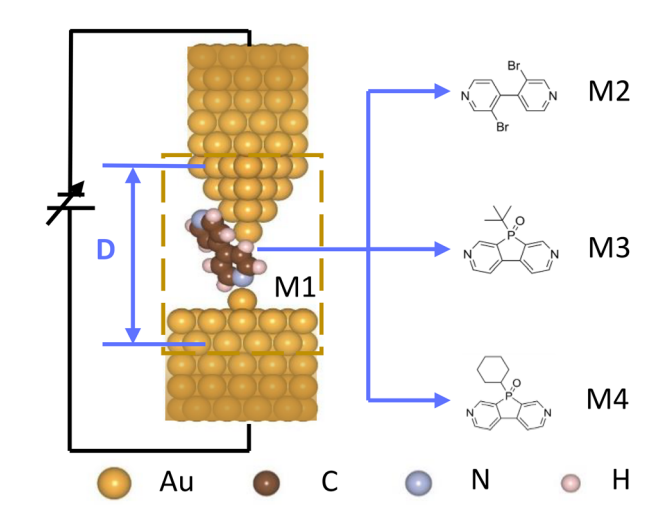


Fig. 1 The schematic structures of 4,4'-bipyridine and its derivative molecular junctions. The structures shown in the rectangular frame are the systems on which we performed *ab initio*-based process calculations. M1 is 4,4'-bipyridine. M2 is 3,3'-dibromo-4,4'-bipyridine. M3 and M4 are two phosphoryl-bridged dipyridyls with methyl and cyclohexyl side substituents, respectively.

and cyclohexyl side substituents, respectively. These molecular junctions have been experimentally studied in our previous work with the STM-BJ technique,<sup>5</sup> which is the common technique used in the studies of dipyridyl molecular junctions.<sup>50–52</sup> In the STM-BJ technique, the gold tip which acts as the upper electrode needs to be fabricated very sharp,2,5 so we use a pyramid-shaped electrode<sup>37</sup> to simulate the tip electrode. As for the substrate, both an Au(111) planar-shaped electrode and a planar-shaped electrode with a single Au atom on the surface are very possible in the experiments. However, for the dipyridyl molecular junctions, only a single Au atom adsorbed on the planar Au(111) surface can sustain a stretching force larger than 1.5 nN. Additionally, in the common formation process of molecular junction by the STM-BJ technique, the tip electrode is first contacted with the substrate electrode to obtain the 1  $G_0$  (1  $G_0 = 2e^2/h$  is the quantum conductance unit) conductance step before forming the molecular junction. 5,50,51 This process makes the tip electrode easily drag a gold atom out of the substrate electrode which then adsorbs on the surface of the substrate electrode. Thus, the Au(111) planar electrode with a single surface Au atom is used to simulate the substrate electrode of the STM-BJ technique in the calculations.

To study the HLCS behaviors and the breaking forces of the dipyridyl molecular junctions, *ab initio*-based adiabatic stretching and compressing simulations are performed. As one knows, the stretching and compressing force  $F = \partial E_J/\partial D \approx \Delta E_J/\Delta D$  is the slope of the single point energy curve *versus* electrode distance (*E*–*D* curve),<sup>57</sup> which is related to the energy variation  $\Delta E_J$  of the molecular junction with the change of the electrode distance  $\Delta D$ . The energy variation is caused by the deformation of the molecular junction which mainly takes place at the molecule and electrode–molecule interfaces. The

Paper Nanoscale

atoms in the bulk electrode are confined by the crystal lattice and the deformation of the bulk electrode is negligible in the stretching and compressing processes. Thus, in the calculations, considering the expensive computational cost and the reliability of the results, it is feasible and reasonable to only consider the systems in the yellow dashed rectangles in Fig. 1.

To obtain the stretching and compressing forces of the molecular junctions, the single point energies for the molecular junctions in the stretching and compressing processes are first computed. According to the literature, one can find that whether measured in air<sup>5,51</sup> or in 1,2,4-trichlorobenzene solution, 50,52 the HLCS phenomena are observed in each case for the pyridyl-anchored molecular junctions and the high and low conductance values are approximately the same for the same molecules. This indicates that the organic solvent of 1,2,4-trichlorobenzene commonly used in the experiment has a very weak effect on the dipyridyl molecular junctions and is negligible relative to the molecule-electrode interaction. Therefore, in the calculations of this work, we do not consider the solvent effects.

The electrode gaps of the molecular junctions are adjusted step by step in the calculations of the stretching and compressing processes. In each step of the geometric optimization, the dipyridyl molecules and the Au atoms in the inner gold layers are fully relaxed, while the Au atoms in the outer layers are fixed to sustain the stretching and compressing forces. For each step, the just-optimized positions of the relaxed atoms in the previous step are taken as the initial geometry to perform further relaxation calculations. In this way, the adiabatic stretching and compressing processes of the molecular junctions are implemented at the B3LYP level with the Lanl2DZ basis set in the Gaussian16 package.<sup>58</sup>

Generally, the biases used in the experimental measurements of dipyridyl molecular junctions are very low ( $V \le 0.3 \text{ V}$ ). For such low bias voltages, no conductive channel opens, thus the electronic transports of the molecular junctions are dominated by non-resonant transmissions. For a non-resonant transmission, the electronic wave is injected into a molecule from one electrode by the bias, which is scattered and diffracted by the potential field of the molecule, and finally enters the other electrode with some probability. To understand the electronic transport dominated by the non-resonant transmission, we developed a one-dimensional transmission combined with a three-dimensional correction approximation (OTCTCA) method.<sup>59</sup> In this method, the current is written as:

$$I = S \int e j_x [f_S(E)\rho_S(E) - f_D(E)\rho_D(E)] T(E) dE$$
 (1)

where  $j_x$  is the probability flux along the transport direction.  $f_{\rm S}(E)$  and  $f_{\rm D}(E)$  are the Fermi distribution functions of the source and drain, respectively.  $\rho_{\rm S}(E)$  and  $\rho_{\rm D}(E)$  are the densities of states of the source and drain, S is the effective incident area of an electronic wave, and T(E) is the electronic transmission probability which depends on the potential field around the molecule (scattering region) and can be approximately obtained by numerically solving the one-dimensional Schrödinger equation

$$-\frac{\hbar^2}{2m}\frac{d^2}{\mathrm{d}x^2}\psi(x) + U(x)\psi(x) = E\psi(x) \tag{2}$$

combined with a three-dimensional correction, where U(x) is the spatial potential field along the transmission paths. In our previous work we only simply calculated T(E) along a straight path.<sup>59</sup> In this work, we optimized the OTCTCA method and developed our code, which can calculate T(E) along curving paths according to the geometries of the molecular junctions.

#### III. Results and discussion

#### A. Contact configuration evolution of dipyridyl molecular junctions

According to the experiments, the low conductance range occurs about 0.2 nm after that of the high conductance for dipyridyl molecular junctions, 5,50 which is quite approximate to the distance between two neighboring Au layers. Thus, one can believe that the HLCS behaviors of the dipyridyl molecular junctions are most likely related to the two topmost layers of the tip electrode, i.e., the top Au atom and the second Au layer. Therefore, in the beginning of the stretching simulations, we put the upper pyridyls beside the second Au layers of the tip electrodes. Fig. 2 shows the configuration evolution of the M1-M4 molecular junctions in the stretching and compressing processes.

The calculations show that the stretching and compressing processes of the M1 and M2 systems are very similar. For the M1 and M2 systems, when the electrode distances (denoted as D in Fig. 1) are less than 2.03 nm (Fig. 2(a) and (e)), the upper pyridyls lean beside the tip electrodes. When the electrode distance is stretched to 2.04 nm, the most distinct phenomena arise, that is the upper pyridyls are approximately vertically adsorbed on the Au atoms of the second layers of the tip electrodes (Fig. 2(b) and (f)). At the same time, the upper pyridyls generate unique lateral-pushing forces which push the top Au atoms of the upper electrodes aside. This contact geometry is very interesting, which is rarely found in the stretching simulations of amino-ended and thiol-ended molecular junctions.<sup>8,37</sup> In the following discussions we denote this contact geometry as a step type contact configuration or for short as the S-type contact. For the S-type contact, besides the Au atom which directly connects with the upper pyridyl, there are also three other Au atoms very close to the upper pyridyl of the molecule, which can give additional pathways for the electrons to transport between the molecule and the electrode. Therefore, the S-type contact is expected to be the most likely contact configuration for the high conductance in the experiment. On further elongating the electrode gaps to D = 2.24 nm, the upper pyridyls are broken from the second Au layers and adsorbed on the top Au atoms of upper electrodes (Fig. 2(c) and (g)), which we named the T-type contact. One can easily see that there is only one Au atom which provides the pathway

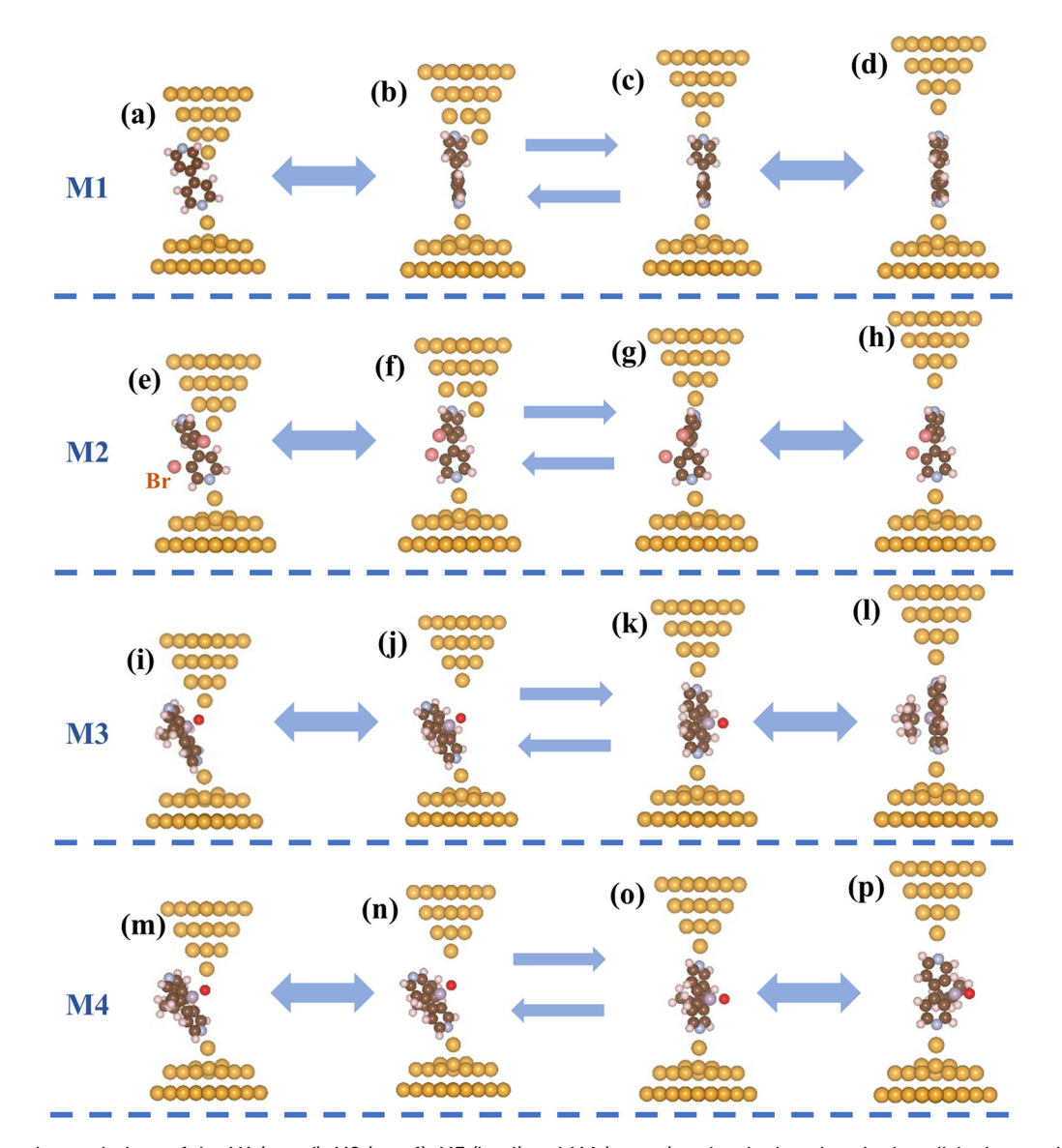


Fig. 2 Configuration evolutions of the M1 (a  $\leftrightarrow$  d), M2 (e  $\leftrightarrow$  f), M3 (i  $\leftrightarrow$  l) and M4 (m  $\leftrightarrow$  p) molecular junctions in the adiabatic stretching and compressing processes. The single head arrows in the figure denote the stretching and compressing processes are irreversible. The double head arrows denote the stretching and compressing processes are reversible.

for the electrons transporting between the molecule and electrodes for the T-type contact configuration, which is evidently narrower than that of the S-type contact. Thus, the T-type contact is expected to correspond to the low-conductance contact configuration. Moreover, based on the calculation, the S-type contact configuration can sustain about 0.21 nm, which is very close to the experimental observations that the low conductance range occurs about 0.2 nm after that of the high conductance.<sup>5,50</sup> On further elongating the electrode distances of the M1 and M2 molecular junctions to about 2.44 nm, the molecular junctions are broken with the upper pyridyls being separated from the tip electrodes (Fig. 2(d) and (h)).

On compressing the electrodes then, the molecular junctions are rebuilt at D = 2.43 nm. However, it needs to compress the electrode distance to 2.13 nm for the upper pyridyls

switching from the top Au atoms to the second Au layers. On further compressing the electrodes to D = 2.03 nm, the upper pyridyls of M1 and M2 are again adsorbed beside the tip electrodes. It should be mentioned that for the electrode distance between 2.14 and 2.24 nm, the stretching and compressing processes of the M1 and M2 molecular junctions are irreversible.

The stretching and compressing processes of the M3 and M4 molecular systems are completely different from those of the M1 and M2 systems. The O atoms bonded on the phosphoryl bridges are the first to adsorb on the top Au atoms as soon as the two electrodes separate from each other (Fig. 2(i) and (m), denoted as the O-type contact). Even when the upper pyridyls of M3 and M4 are near the second Au layers of the tip electrodes for 2.03 nm < D < 2.23 nm, the adsorption between

Paper Nanoscale

O and the top Au atoms always hinder the pyridyls from adsorbing on the second gold layers. Until the O atoms are far enough away from the top Au atoms for D > 2.32 nm, the pyridyls directly adsorb on the top Au atoms (Fig. 2(k) and (o)) instead of on the second Au layers of the tip electrodes. When compressing the M3 and M4 molecular junctions from a large electrode distance, the upper pyridyls glide to the side positions of the tip electrodes at D = 2.17 nm. In the compressing processes of the M3 and M4 molecular junctions, the upper pyridyls still cannot connect with the second Au layers of the tip electrodes due to the hindrance of the interactions between O atoms and the top Au atoms. Thus, the calculations reveal that it is not according to previous expectations that the bulky methyl and cyclohexyl side-groups sterically hinder the M3 and M4 molecular systems from converting their contact configurations,<sup>5</sup> but the O atoms tend to first adsorb on the top Au atoms and hinder the molecular systems from adopting the S-type contact configuration.

#### B. Energy and force traces of dipyridyl molecular junctions in the stretching and compressing processes

Fig. 3 shows the energy and force traces for the M1–M4 molecular junctions in the stretching and compressing processes. The figure shows that, for the M1 and M2 systems, the minimum energy states for the upper pyridyls adsorbing

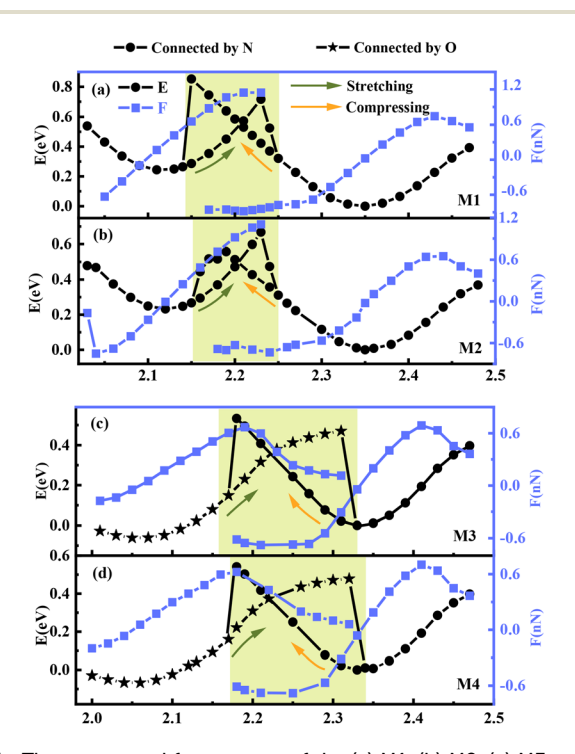


Fig. 3 The energy and force traces of the (a) M1, (b) M2, (c) M3 and (d) M4 molecular junctions in the adiabatic stretching and compressing processes. The yellow shaded area indicates the electrode distance where irreversible contact conformational evolution occurs during stretching and compression. The orange arrows indicate the compressing process, and the gray arrows indicate the stretching process.

on the second Au layers present at D = 2.12 nm. However, for the upper pyridyls adsorbing on the top Au atoms of upper electrodes, the minimum energy occurs at about 2.35 nm, which is about 0.23 nm after that of the upper pyridyls adsorbing on the second Au layers. For the M3 and M4 molecular junctions, the electrode distances of minimum energy for the O atoms adsorbing on the top Au atoms are at about 2.06 and 2.05 nm respectively, which are evidently shorter than those of the upper pyridyls adsorbing on the second Au layers for the M1 and M2 systems. Thus, when fabricating M3 and M4 molecular junctions, before the upper pyridyls can adsorb on the second Au layers, the O atoms have already adsorbed on the tip Au atoms. Fig. 3(c) and (d) also show that, for the M3 and M4 systems, the minimum energy for the upper pyridyls adsorbing on the top Au atoms is at about 2.33 nm, which is just after the O atoms have broken from the top Au atoms, thus the upper pyridyls can only adsorb on the top Au atoms instead of on the second gold layers. It should be noticed that the minimum energies for the upper pyridyls adsorbing on the second Au layers are about 0.2 eV higher than that of those adsorbing on the top Au atoms for the M1 and M2 systems. However, for the M3 and M4 systems, the minimum energies for O atoms adsorbing on the top Au atoms are about 0.1 eV lower than those of the pyridyls adsorbing on the top Au atoms. These energy differences further demonstrate that, in the stretching processes of the M3 and M4 systems, the O atoms prefer to first adsorb on the top Au atoms and hinder the pyridyls from adsorbing on the second Au layers.

It is noticeable that the calculated stretching force for the upper pyridyl switching from the second Au layer to the top Au atom for the M1 molecular system is up to 1.2 nN, which is evidently larger than 0.8 nN, the force for the pyridyl finally breaking from the top Au atom (Fig. 3(a)). This result is well consistent with the experimental observations that the maximum forces for the high conductance states are larger those for the molecular junctions completely breaking, 51,56 which highly suggests that the high conductance state corresponds to the pyridyl approximately vertically adsorbing on the second Au layer of the tip electrode. For the M2 system, the force for the upper pyridyl breaking from the second Au layer is about 1.1 nN (Fig. 3(b)), which is a little smaller than that of the M1 system due to the substituent of Br atom slightly weakening the coupling between the pyridyl and the tip electrode. For the M3 and M4 systems, despite the O atoms tending to adsorb on the top Au atoms at first, the force for O atoms breaking from the gold tips is only about 0.6 nN (Fig. 3(c) and (d)), which is evidently smaller than that of the pyridyls breaking from the second Au layers. The final breaking force for the M2, M3 and M4 systems is about 0.7 nN for all, which is also a little smaller than that of the M1 system due to the large electronegative substituent atoms (Br or O) in the molecules.

#### C. HLCS behaviors of dipyridyl molecular junctions

To verify whether the HLCS behaviors of the M1 and M2 molecular systems resulted from the configuration conver-

Nanoscale Paper

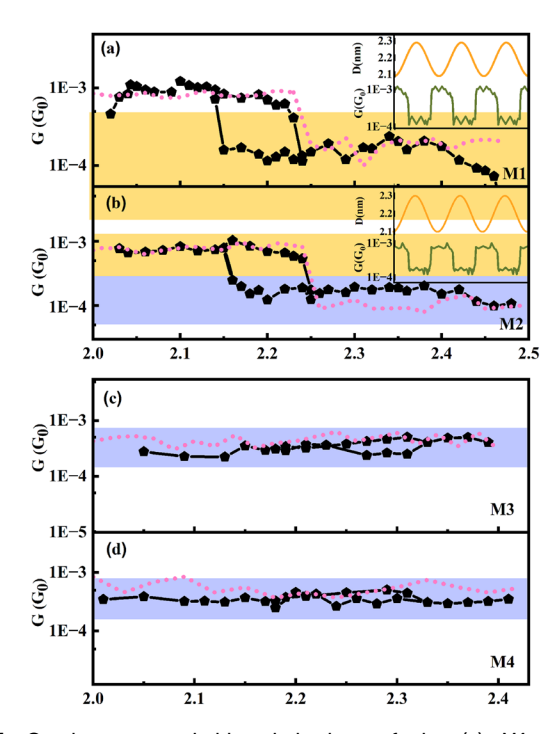


Fig. 4 Conductance switching behaviors of the (a) M1 and (b) M2 molecular junctions during adiabatic stretching and compressing processes. The insets of (a) and (b) show the repeated conductance switching behaviors of the M1 and M2 molecular junctions with the electrodes being repeatedly stretched and compressed. (c) and (d) Conductance traces of the M3 and M4 molecular junctions in the adjabatic stretching and compressing processes. The black solid lines represent the conductance calculated using the OTCTCA method, and the pink dashed lines are the conductance measured in the experiment. 5,50

sions between the S-type and T-type contacts, we further show the conductance traces of the M1-M4 molecular junctions during the stretching and compressing processes in Fig. 4. The figure shows that the M1 and M2 molecular junctions show distinct HLCS behaviors in both the stretching and compressing processes. In particular, the high-low conductance ratios are almost up to an order of magnitude as we observed in the experiment. It is noticeable that the high conductance corresponds to the S-type contact configuration, and the low conductance corresponds to the T-type contact configuration (Fig. 4(a) and (b)). Therefore, it needs larger forces for the M1 and M2 systems to switch from higher conductance to lower conductance and needs smaller forces to break the molecule systems, are well consistent with the experimental measurements. 5,50,51 The inserts of Fig. 4(a) and (b) show the conductance of the M1 and M2 systems with the electrode gaps being repeatedly stretched and compressed between 2.10 nm and 2.30 nm. As we have observed in the experiment, 5,50 the conductance cyclically switches between high and low values perfectly by repeatedly stretching and compressing the M1 and M2 molecular junctions. For the M3 and M4 molecular systems, the conductance for the O atoms adsorbing on the tip Au atoms are very close to those of the T-type contact configuration (Fig. 4(c) and (d)). Therefore,

although there are configuration conversions in the stretching and compressing process of the M3 and M4 systems, no conductance switching behaviors can be found in the experiments for these two systems. These results further clarify that it is not the bulky methyl and cyclohexyl side-groups<sup>5</sup> but the O atoms in the side group prevent the molecules from adopting the "high" conductance geometries and switch off the HLCS behaviors of the M3 and M4 molecular junctions.

The conductance differences between different contact configurations are easily understood from the mechanism of nonresonant electronic transport according to our OTCTCA calculations.<sup>59</sup> In lower bias regimes (≤0.3 V), no resonant transmission channel is opened, thus the conductance of the molecular junction is dominated by non-resonant electronic transmission. For non-resonant transmission, each atom in the molecule produces a potential well around its nucleus, which acts as a micro-hole for the electronic wave. Thus, the electronic wave that is transmitted through the molecules is scattered and diffracted by the atoms in the molecule. Additionally, in the transmission path, the electronic wave can also be reflected due to the rise and fall of the potential field. Thereby, for the non-resonant electronic transport in a molecular junction, after being injected into the molecule region from one electrode by the driving of the bias voltage, the electronic wave is scattered, diffracted and reflected by the potential field around the molecule, and finally enters the other electrode with a certain probability.

As to the dipyridyl molecular junctions with the T-type contact configuration, the scattering, reflection and diffraction effects of the top Au atom on the electronic waves can significantly reduce the transmission probability of electronic waves compared with that of the S-type contact configuration. In the low bias regime, the effective incident energy of the electronic wave is very low, thus the s partial wave governs the scattering. Due to the spherical symmetry of the s partial wave, when the electrons pass through each atom, only a half of the electrons are scattered forward. In addition, the reflection effect (onedimension effect along the transmission pathway) and diffraction effect further reduce the proportion of the forward electrons. According to our computations, due to the scattering, reflection and diffraction of the top Au atom, only about 1/4th of the electronic waves can continue their transmission forward.

Besides the scattering, reflection and diffraction effects of the top Au atom which dominate the high-low conductance ratio, the coupling between the molecule and electrodes also influences the high-low conductance ratio, which can be directly exhibited by the spatial distributions of the occupied molecular orbitals (OMOs). For example, Fig. 5 shows the OMOs which are both delocalized on the tip electrodes and molecules for the M2 and M3 molecular junctions. One can see that, there are 16 delocalized OMOs for the M2 system with the S-type contact configuration. However, for the systems with the T-type contact configuration, there are only 8 delocalized OMOs. The OMOs highly indicate that the coupling between the tip electrode and the molecule for the S-type

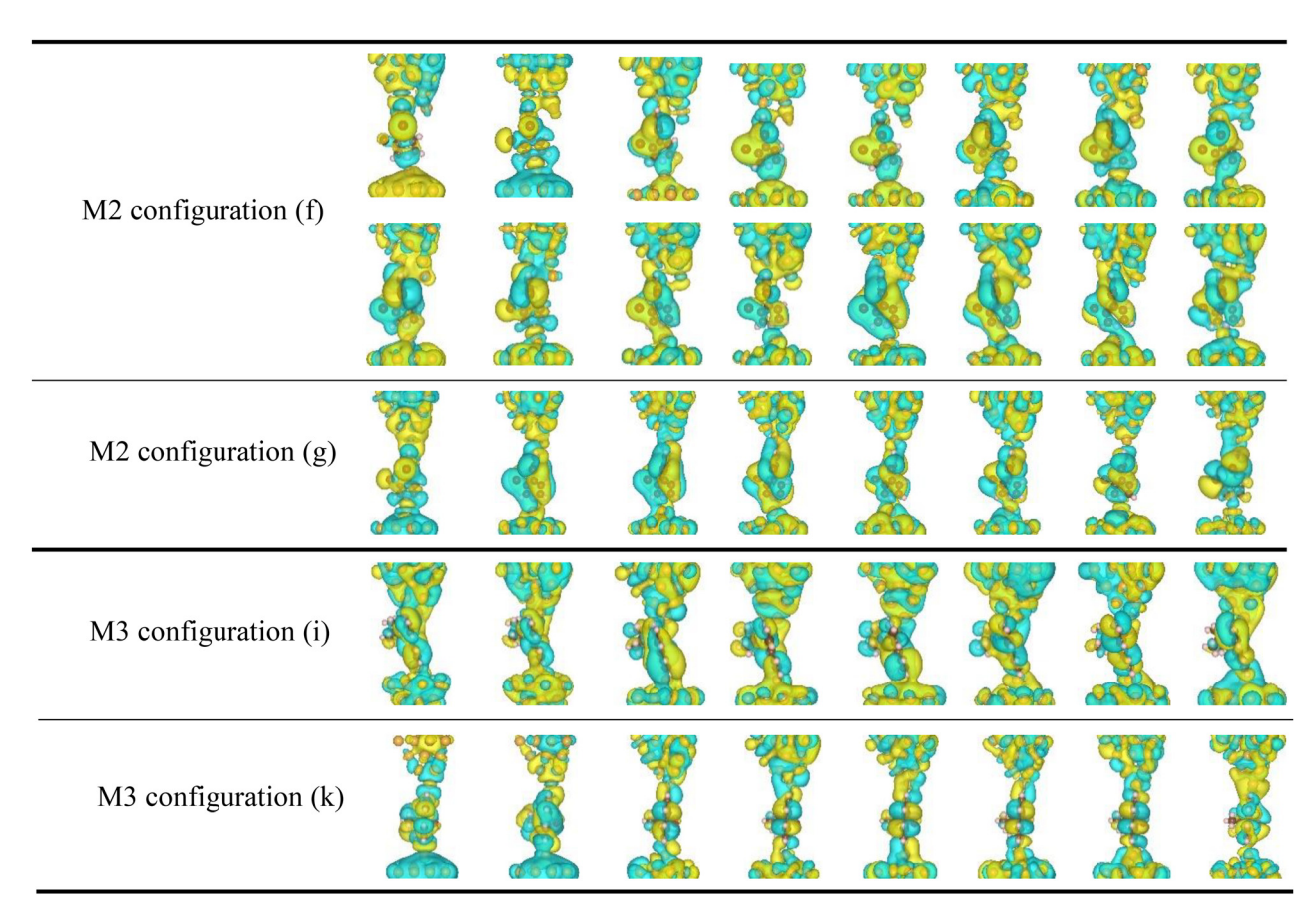


Fig. 5 Spatial distributions of the occupied molecular orbitals (OMOs) which both delocalized on the tip electrodes and molecules for the M2 and M3 systems. There are 16 delocalized OMOs for M2 with the conformation (f) and 8 delocalized OMOs for M2 with the conformation (g). For the M3 system with conformations (i) and (k), there are both 8 delocalized OMOs simultaneously delocalized on the tip electrodes and molecules.

contact configuration is evidently tighter than that of the T-type contact configuration. Thus, the high-low conductance ratios of the M2 system as well as of the M1 system are further enhanced by the influence of the electrode-molecule coupling. However, for the M3 system, the number of delocalized OMOs for the O-type contact configuration is equal to that for the T-type contact configuration. Therefore, the couplings between the tip electrode and M3 molecule for these two configurations are very close to each other, which are also reflected by the breaking forces presented in Fig. 3.

In fact, the electrode-molecule coupling first modulates the spatial distribution of the potential field around the electrode-molecule contact, which further affects the electronic transport. Thus, to gain deep insights into the HLCS behaviors of dipyridyl molecular junctions, we show the spatial distribution of the potential fields of the M2 and M3 molecular systems in Fig. 6. Herein the dashed blue rectangles denote the contact areas between the upper pyridyls and the tip electrodes. The thick green lines are the boundaries of the potential well areas, and the thick black lines are the boundaries of the lower potential barrier areas for the electrons. The figure shows that, for the M2 system with the S-type contact configuration (Fig. 6(a)), there is an evident potential well channel connected

between the molecule and the tip electrode in the upper contact region. Moreover, the range of the lower potential barrier around the upper contact area is very wide, which significantly enhances the probability of the electronic transmission between the molecule and electrode. However, for the T-type contact configuration (Fig. 6(b)), not only the potential well channel but also the lower potential barrier range around the upper contact area are both much narrower than that of the S-type contact configuration. Thus, for the system with the T-type contact configuration, the tip Au atom not only gives additional scattering to the transmission of the electronic waves, but at the same time provides a much narrower transmission channel for the electrons transmitting between the tip electrode and molecule, which dramatically suppresses the electronic transport. For the M3 system, the transmission path of the molecular junction with the O-type contact configuration (Fig. 6(c)) seems shorter than that of the T-type contact configuration (Fig. 6(d)), but due to the strong electronegativity of the O atom, the incident cross-sectional area for the O atom adsorbing on the tip Au atom is less than that of the T-type contact configuration, which thus decreases the probability of the incident electronic waves and further the conductance. Therefore, the conductance for the system with the O-type

Nanoscale Paper

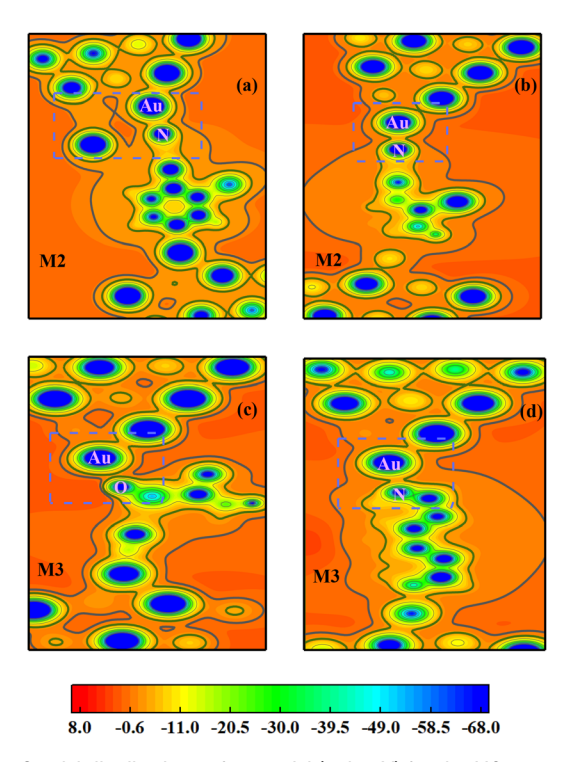


Fig. 6 Spatial distributions of potential (unit: eV) for the M2 system with pyridyl anchoring on (a) the second Au layer of electrode tip and (b) the tip Au atom of electrode. Spatial distributions of potential for the M3 system with (c) O atom adsorbing on the tip Au atom and (d) pyridyl anchoring on the tip Au atom of the electrode. The dashed blue rectangles denote the contact areas between the upper pyridyls and the tip electrodes. The thick green lines are the boundaries of the potential wells for the electronic transports, and the thick black lines denote the lower potential barrier areas for the electrons.

contact configuration is approximately equal to that of a system with the T-type contact configuration and no HLCS behaviors arise for the M3 and M4 systems.

It should be mentioned that based on the knowledge of quantum mechanics and the OTCTCA method, the electronic wave transports as a decaying wave when it transmits through a potential barrier region, thus the transmission probability approximately exponentially decays with the increase of the length and height of the potential barrier. However, the electronic wave transports as a plane wave in the potential well region, which can be reflected by the ups and downs of the potential wells but does not decay with the increase of the depth and length of the potential well. Therefore, if the atom number is unchanged in the transmission path, the stretching and the compressing of the molecular junction generally have a little influence on the conductance of the molecular system. That is why the conductance traces often show steplike features in the forming processes of molecular junctions. 37,59 As conductance commonly shows a sharp skip between two neighboring conductance steps, it generally results from the abrupt inelastic deformations of the contact configuration or an abrupt break in the stretching and compressing processes of molecular junction, which respectively changes the number of the scattering centers or the width of the potential barriers during a very short time.

#### D. Discussion

There still exist some questions worthy of consideration. One is that whether the contact configurations discussed above are formed most probably or just accidentally? Obviously, according to the STM-BI technique, both planar electrodes and planar electrodes with a single Au atom on their surface are very common for the substrate electrode in the experiments. Our calculations show that for the pyridyl-terminated molecule adsorbing on the planar electrode, the molecule is directly pulled away from the planar electrode by the tip electrode with the pulling force of only about 0.3-0.5 nN, which is too small to change the contact configuration between the pyridyl and tip electrode. 60 Thus, the HLCS behavior could not have arisen for the dipyridyl molecule adsorbing on the planar substrate. When the lower pyridyl links with the single Au atom which adsorbed on the planar electrode surface as shown in Fig. 1, it can sustain about 1.7 nN stretching force. This force is enough to change the contact configuration between the pyridyl and tip electrode and further sustain the breaking force that the experiment showed (0.8-1.5 nN). 51,56 Thus one can confirm that the planar-shaped electrode with a single surface Au atom is the most probable configuration for the substrate electrode to produce HLCS behaviors.

The tip electrode generally needs to be fabricated very sharp in the experiment. It may be fabricated with various configurations in the actual experiments. However, the common process that the tip electrode is first contacted with the substrate electrode to obtain the 1  $G_0$  conductance step before forming a molecular junction<sup>5,50,51</sup> makes it easy to produce a sharp gold tip due to the traction between the tip electrode and substrate electrode. At least the top Au atom and the second Au layers form a sharp gold tip, which is enough to ensure the HLCS behaviors of dipyridyl molecular junctions. The calculations show that more Au atoms in the third and fourth Au layers have little effect on the electronic transport properties and further the HLCS behaviors of dipyridyl molecular junctions. Considering that too many Au atoms in the ab initio calculations cannot evidently enhance the accuracy of the calculated HLCS behaviors of the dipyridyl molecular junctions, but only result in unbearable computational cost, we only use more gold atoms to verify the reliability of our calculations in the test computations.

The choice of different electrode sizes in the computations does result in different single point energies of the molecular junction. However, considering that the stretching and compressing forces are simultaneously related to the energy changes of the system and the changes of the electrode distance, at the same time based on the principle of transitivity of forces, one can understand that the choice of the electrode size almost does not affect the numerical result of the stretching and compressing forces of the molecular junction. Therefore, the choice of the electrode size mainly depends on the deformation range of the molecular junction which governs the variation of the conductance of the molecular junction. In fact, the zero-point vibrational energy

Paper Nanoscale

can produce a correction to the stretching and compressing forces of the molecular junction, but based on our knowledge, which only brings a correction of less than 0.02 nN for the breaking force.<sup>57</sup> Thus, in this work the effect of zero-point vibrational energy on the stretching and compressing forces is not considered.

According to the previous investigations, 50,51 the HLCS behavior of dipyridyl molecular junctions is attributed to the change of the angle between the N-Au bond and the  $\pi$  system with the change of the electrode-electrode separation. However, in those investigations, the deformation processes of the gold electrodes near the electrode-molecule contacts were not considered, thus the specific contact configuration produced in the stretching and compressing processes of the dipyridyl molecular junction, i.e., the S-type contact configuration, could not be found. Therefore, the questions that we mentioned in the Introduction section, especially questions (2) and (3) are difficult to understand. In our studies, large quantities of ab initio computations are performed to particularly consider the deformation of the electrode tips during the stretching and compressing of dipyridyl molecular junctions, therefore the specific deformations of the electrode tip are perfectly decoded as well as the evolution processes of electrodemolecule contact configurations, thus the above questions are easily solved. Additionally, based on the change of the angle between the N-Au bond and the  $\pi$  system, the question why the low conductance ranges occur about 0.2 nm after the break of the gold point contact<sup>5,50</sup> is also difficult to understand. However, because the distance between the two neighboring Au layers is about 0.23 nm, one can easily understand this question by comparing the T-type configuration with the S-type configuration. Based on the above discussions one can expect that, for longer pyridyl-ended molecule, the high conductance plateau may much wider than 0.2 nm because the upper pyridyl can first adsorb on the third Au layer of the tip electrode after the gold contact being broken, which is consistent with the results of literature reports<sup>51,55</sup> and is verified by our recent observations. Our simulations indicate that the ab initio-based adiabatic simulation method is very useful in decoding the specific contact configurations as well as the formation processes of molecular junctions.

Then we discuss why do we use OTCTCA method to calculate the electronic transports in dipyridyl molecular junctions. As one knows, for different kinds of molecular or nano junctions in different bias regimes, the mechanisms which dominate the electronic transport are different. Generally, the current through the junctions is calculated by Landauer-Büttiker formula.<sup>61</sup> However, by applying non-equilibrium Green's function (NEGF) method,<sup>62</sup> the local current in molecular wires can be computed exactly. 63-68 For donor-acceptor (D-A) blending systems, such as D-A mixed-stack organic cocrystals or D-A copolymers, where the electron transport between two electrodes cannot be accomplished by a single molecular orbital, then a long-range superexchange mechanism plays an important role in charge transfer which relies on the superexchange coupling between the adjacent donor

and acceptor moieties. For the superexchange mechanism, the acceptor acts as a bridge for the electron to hop between donor sites and the donor acts as a bridge for the hole to hop between acceptor sites. 69-74 The superexchange model is also a simple atomistic model of tunneling through molecules. 75,76 However, for the small dipyridyl molecular junctions at lower bias voltages, there is no conductance channel entering the bias window and non-resonant electron transport dominates electron transport. Although exact approaches for the calculation of local currents are available, 69-74 here we rely on a simpler approximate consideration of OTCTCA which should be enough for our purposes. For the OTCTCA method, the spatial distribution of the potential field around the molecular junction is first calculated which contains a series of potential wells and potential barriers as shown in Fig. 6. Then the T(E), which is the statistical electronic transmission probability for the electrons transport through a series of transmission paths, is calculated by numerically solving a series of one-dimensional Schrödinger equations. In the calculations of T(E), a three-dimensional correction is considered according to the characteristics of a low-energy s partial wave, 59 which significantly enhances the accuracy of the numerical results. Based on our OTCTCA method, the conductance of the molecular system is more sensitive to the number of scattering centers (general the number of atoms) in the transmission path (see Fig. 6) than the energy level alignments. Therefore, the OTCTCA method is only feasible for short-molecule junctions at lower bias voltages.

The solvent effects are another issue that should be discussed further. In order to reveal why the HLCS behaviors of dipyridyl molecular junctions are almost independent of the commonly used 1,2,4-trichlorobenzene solvent, 50,52 we take 4,4'-bipyridine molecular junction as an instance to perform further geometric optimizations with the 1,2,4-trichlorobenzene molecules next to the N-Au contacts. The calculations show that the 1,2,4-trichlorobenzene molecules move away from the N-Au contacts, which leads the effect of the 1,2,4-trichlorobenzene molecules on the molecule-electrode interaction and the spatial potential distribution along the backbone of the molecular junction is very weak. Numerical results show that the force differences between 4,4'-bipyridine molecular junctions with and without 1,2,4-trichlorobenzene molecules do not exceed 0.01 nN, which is much smaller than the breaking forces (about 0.6-1.5 nN) of the molecular junctions. Thus, the HLCS behaviors of dipyridyl molecular junctions are little affected by the 1,2,4-trichlorobenzene solvent. One might assume that the H2O molecules readily form hydrogen bonds with the N atoms of the dipyridyl molecule and can significantly affect the electronic transport of the molecular junction, but the 4,4'-bipyridine molecular junction exhibits a similar HLCS behavior in aqueous solution.<sup>77</sup> Our calculations show that the hydrogen bonds between the N atoms and the H2O molecules cannot hinder the dipyridyl molecule from vertically adsorbing on the second layer of the tip gold electrode. Thus, the dipyridyl molecular junctions exhibit similar HLCS behaviors whether in water, in 1,2,4-trichlorobenzene or in air.

Paper

#### IV. Conclusion

The stretching and compressing processes and the HLCS behaviors of dipyridyl molecular junctions are investigated by applying the ab initio-based adiabatic process simulation method. The numerical simulations revealed that during the stretching and compressing processes of dipyridyl molecular junctions, the pyridyls tend to push the top Au atoms aside and approximately vertically adsorb on the second Au layers of the tip electrodes, which brings stronger molecule-electrode coupling and larger incident sectional areas for electronic waves and further results in large breaking forces and high conductance of the molecular junctions. However, when the pyridyls are further stretched to adsorb on the top Au atoms of the tip electrode, the top Au atoms produce additional scattering of the electrons. Meanwhile, both the molecule-electrode couplings and the electronic incident cross-sectional areas are decreased, which leads to small breaking forces and low conductance of the molecular junctions. The O atoms in the phosphoryl bridged between two pyridyls prefer to adsorb first on the tip Au atoms, which hinders the pyridyl from adsorbing on the second Au layers and results in a low conductance state, thus the switching behaviors of the molecular junctions are inhibited.

#### **Author contributions**

Feng Sun and Lin Liu performed the calculations and the data analysis and wrote the original draft. Chang-Feng Zheng, Yu-Chen Li, Yan Yan and Xiao-Xiao Fu discussed the results and reviewed the manuscript. Ran Liu, Bingqian Xu and Zong-Liang Li contributed the ideas and discussed the manuscript in detail. Ran Liu and Zong-Liang Li developed the method and wrote the manuscript. Feng Sun, Chuan-Kui Wang, Ran Liu, Bingqian Xu and Zong-Liang Li revised and reviewed the final manuscript.

#### Conflicts of interest

There are no conflicts to declare.

### Acknowledgements

This work is supported by the National Natural Science Foundation of China (Grant No. 11974217, 11874242 and 11804197) and the US National Science Foundation (ECCS 1231967 and 2010875).

#### References

- 1 M. A. Reed, C. Zhou, C. J. Muller, T. P. Burgin and J. M. Tour, *Science*, 1997, 278, 252–254.
- 2 B. Q. Xu and N. J. Tao, Science, 2003, 301, 1221-1223.

- 3 B. Q. Xu, X. L. Li, X. Y. Xiao, H. Sakaguchi and N. J. Tao, Nano Lett., 2005, 5, 1491–1495.
- 4 A. Vezzoli, I. Grace, C. Brooke, K. Wang, C. J. Lambert, B. Q. Xu, R. J. Nichols and S. J. Higgins, *Nanoscale*, 2015, 7, 18949–18955.
- 5 A. K. Ismael, K. Wang, A. Vezzoli, M. K. Al-Khaykanee, H. E. Gallagher, I. M. Grace, C. J. Lambert, B. Q. Xu, R. J. Nichols and S. J. Higgins, *Angew. Chem.*, *Int. Ed.*, 2017, 56, 15378–15382.
- 6 D. Xiang, H. Jeong, D. Kim, T. Lee, Y. J. Cheng, Q. L. Wang and D. Mayer, *Nano Lett.*, 2013, **13**, 2809–2813.
- 7 D. Xiang, X. L. Wang, C. C. Jia, T. Lee and X. F. Guo, *Chem. Rev.*, 2016, **116**, 4318–4440.
- 8 R. Liu, Y. M. Han, F. Sun, G. Khatri, J. Kwon, C. Nickle, L. J. Wang, C. K. Wang, D. Thompson, Z. L. Li, C. A. Nijhuis and E. del Barco, *Adv. Mater.*, 2022, 34, 2202135.
- 9 C. C. Jia, A. Migliore, N. Xin, S. Y. Huang, J. Y. Wang, Q. Yang, S. P. Wang, H. L. Chen, D. M. Wang, B. Y. Feng, Z. R. Liu, G. Y. Zhang, D. H. Qu, H. Tian, M. A. Ratner, H. Q. Xu, A. Nitzan and X. F. Guo, *Science*, 2016, 352, 1443– 1445.
- 10 X. M. Xie, P. H. Li, Y. X. Xu, L. Zhou, Y. H. Yan, L. H. Xie, C. C. Jia and X. F. Guo, ACS Nano, 2022, 16, 3476–3505.
- 11 C. L. Guo, K. Wang, E. Zerah-Harush, J. Hamill, B. Wang, Y. Dubi and B. Q. Xu, *Nat. Chem.*, 2016, 8, 484–490.
- 12 H. Y. Fu, F. Sun, R. Liu, Y. Q. Suo, J. J. Bi, C. K. Wang and Z. L. Li, *Phys. Lett. A*, 2019, **383**, 867–872.
- 13 L. L. Niu, H. Y. Fu, Y. Q. Suo, R. Liu, F. Sun, S. S. Wang, G. P. Zhang, C. K. Wang and Z. L. Li, *Phys. E*, 2021, 128, 114542.
- 14 P. Jiang, G. M. Morales, W. You and L. P. Yu, *Angew. Chem.*, *Int. Ed.*, 2004, **43**, 4471–4475.
- 15 S. Zhang, C. Guo, L. Ni, K. M. Hans, W. Zhang, S. Peng, Z. Zhao, D. C. Guhr, Z. Qi, H. Liu, M. Song, Q. Wang, J. Boneberg, X. Guo, T. Lee, E. Scheer and D. Xiang, *Nano Taday*, 2021, 39, 101226.
- 16 Y. P. Zhang, L. C. Chen, Z. Q. Zhang, J. J. Cao, C. Tang, J. Y. Liu, L. L. Duan, Y. Huo, X. F. Shao, W. J. Hong and H. L. Zhang, J. Am. Chem. Soc., 2018, 140, 6531–6535.
- 17 L. N. Meng, N. Xin, C. Hu, J. Y. Wang, B. Gui, J. J. Shi, C. Wang, C. Shen, G. Y. Zhang, H. Guo, S. Meng and X. F. Guo, *Nat. Commun.*, 2019, 10, 1450.
- 18 N. Xin, J. Y. Wang, C. C. Jia, Z. T. Liu, X. S. Zhang, C. M. Yu, M. L. Li, S. P. Wang, Y. Gong, H. T. Sun, G. X. Zhang, Z. R. Liu, G. Y. Zhang, J. H. Liao, D. Q. Zhang and X. F. Guo, *Nano Lett.*, 2017, 17, 856–861.
- 19 M. del Valle, R. Gutiérrez, C. Tejedor and G. Cuniberti, *Nat. Nanotechnol.*, 2007, **2**, 176–179.
- 20 D. Nozaki and G. Cuniberti, Nano Res., 2009, 2, 648-659.
- 21 T. Brumme, O. A. Neucheva, C. Toher, R. Gutiérrez, C. Weiss, R. Temirov, A. Greuling, M. Kaczmarski, M. Rohlfing, F. S. Tautz and G. Cuniberti, *Phys. Rev. B: Condens. Matter Mater. Phys.*, 2011, 84, 115449.
- 22 B. Q. Xu, X. Y. Xiao, X. M. Yang, L. Zang and N. J. Tao, J. Am. Chem. Soc., 2005, 127, 2386–2387.

Paper

- 23 Z. L. Li, X. X. Fu, G. P. Zhang and C. K. Wang, Chin. J. Chem. Phys., 2013, 26, 185-190.
- 24 W. Y. Su, J. Jiang, W. Lu and Y. Luo, Nano Lett., 2006, 6, 2091-2094.
- 25 Q. L. Wang, R. Liu, D. Xiang, M. Y. Sun, Z. K. Zhao, L. Sun, T. T. Mei, P. F. Wu, H. T. Liu, X. F. Guo, Z. L. Li and T. Lee, ACS Nano, 2016, 10, 9695-9702.
- 26 Z. L. Jiang, H. Wang, Y. F. Wang, S. Sanvito and S. M. Hou, J. Phys. Chem. C, 2017, 121, 27344-27350.
- 27 Z. L. Li, J. J. Bi, R. Liu, X. H. Yi, H. Y. Fu, F. Sun, M. Z. Wei and C. K. Wang, Chin. Phys. B, 2017, 26, 098508.
- 28 W. K. Zhao, D. Q. Zou, Z. P. Sun, Y. J. Yu and C. L. Yang, Phys. Lett. A, 2018, 382, 2666-2672.
- 29 F. Schedin, A. K. Geim, S. V. Morozov, E. W. Hill, P. Blake, M. I. Katsnelson and K. S. Novoselov, Nat. Mater., 2007, 6, 652-655.
- 30 M. Zhou, Y. H. Lu, Y. Q. Cai, C. Zhang and Y. P. Feng, Nanotechnology, 2011, 22, 385502.
- 31 S. S. Wang, Z. Yang, F. Sun, R. Liu, L. Liu, X. X. Fu, C. K. Wang and Z. L. Li, J. Phys. Chem. C, 2021, 125, 27290-27297.
- 32 Y. X. Zhu, Z. B. Tan and W. J. Hong, ACS Omega, 2021, 6, 30873-30888.
- 33 Z. Zhao, C. Guo, L. Ni, X. Zhao, S. Zhang and D. Xiang, Nanoscale Horiz., 2021, 6, 386-392.
- 34 J. M. Hamill, K. Wang and B. Q. Xu, Nanoscale, 2014, 6,
- 35 W. J. Hong, D. Z. Manrique, P. Moreno-García, M. Gulcur, A. Mishchenko, C. J. Lambert, M. R. Bryce and T. Wandlowski, J. Am. Chem. Soc., 2012, 134, 2292-2304.
- 36 R. Liu, J. J. Bi, Z. Xie, K. K. Yin, D. Y. Wang, G. P. Zhang, D. Xiang, C. K. Wang and Z. L. Li, Phys. Rev. Appl., 2018, 9, 054023.
- 37 Z. K. Zhao, R. Liu, D. Mayer, M. Coppola, L. Sun, Y. S. Kim, C. K. Wang, L. F. Ni, X. Chen, M. N. Wang, Z. L. Li, T. Lee and D. Xiang, Small, 2018, 14, 1703815.
- 38 Z. L. Li, B. Zou, C. K. Wang and Y. Luo, Phys. Rev. B: Condens. Matter Mater. Phys., 2006, 73, 075326.
- 39 T. Kühne, K. H. Au-Yeung, F. Eisenhut, O. Aiboudi, D. A. Ryndyk, G. Cuniberti, F. Lissel and F. Moresco, Nanoscale, 2020, 12, 24471-24476.
- 40 Z. C. Pan, L. C. Chen, C. Tang, Y. Hu, S. S. Yuan, T. Y. Gao, J. Shi, J. Shi, Y. Yang and W. J. Hong, Small, 2022, 18, 2107220.
- 41 M. Frei, S. V. Aradhya, M. S. Hybertsen and L. Venkataraman, J. Am. Chem. Soc., 2012, 134, 4003–4006.
- 42 C. Li, I. Pobelov, T. Wandlowski, A. Bagrets, A. Arnold and F. Evers, J. Am. Chem. Soc., 2008, 130, 318-326.
- 43 K. Wang, A. Vezzoli, I. M. Grace, M. McLaughlin, R. J. Nichols, B. Q. Xu, C. J. Lambert and S. J. Higgins, Chem. Sci., 2019, 10, 2396-2403.
- 44 C. R. Arroyo, E. Leary, A. Castellanos-Gómez, G. Rubio-Bollinger, M. T. González and N. Agraït, J. Am. Chem. Soc., 2011, 133, 14313-14319.
- 45 F. Chen, X. L. Li, J. S. Hihath, Z. F. Huang and N. J. Tao, J. Am. Chem. Soc., 2006, 128, 15874-15881.

- 46 D. Xiang, T. Lee, Y. Kim, T. Mei and Q. Wang, Nanoscale, 2014, 6, 13396-13401.
- 47 S. Yuan, X. Xu, A. Daaoub, C. Fang, W. Cao, H. Chen, S. Sangtarash, J. Zhang, H. Sadeghi and W. Hong, Nanoscale, 2021, 13, 12594-12601.
- 48 J. F. Zhou, K. Wang, B. O. Xu and Y. Dubi, J. Am. Chem. Soc., 2018, **140**, 70-73.
- 49 P. Zhou, J. Zheng, T. Han, L. Chen, W. Cao, Y. Zhu, D. Zhou, R. Li, Y. Tian, Z. Liu, J. Liu and W. Hong, Nanoscale, 2021, 13, 7600-7605.
- 50 S. Y. Quek, M. Kamenetska, M. L. Steigerwald, H. J. Choi, S. G. Louie, M. S. Hybertsen, J. B. Neaton and L. Venkataraman, Nat. Nanotechnol., 2009, 4, 230-234.
- 51 S. V. Aradhya, M. Frei, M. S. Hybertsen L. Venkataraman, Nat. Mater., 2012, 11, 872-876.
- 52 T. Kim, P. Darancet, J. R. Widawsky, M. Kotiuga, S. Y. Quek, J. B. Neaton and L. Venkataraman, Nano Lett., 2014, 14, 794-798.
- 53 G. Mezei, Z. Balogh, A. Magyarkuti and A. Halbritter, J. Phys. Chem. Lett., 2020, 11, 8053-8059.
- 54 A. Magyarkuti, Z. Balogh, G. Mezei and A. Halbritter, J. Phys. Chem. Lett., 2021, 12, 1759-1764.
- C. Whalley, 55 M. Kamenetska, S. Y. Quek, A. M. L. Steigerwald, H. J. Choi, S. G. Louie, C. Nuckolls, M. S. Hybertsen, J. B. Neaton and L. Venkataraman, J. Am. Chem. Soc., 2010, 132, 6817-6821.
- 56 B. Q. Xu, X. Y. Xiao and N. J. Tao, J. Am. Chem. Soc., 2003, 125, 16164-16165.
- 57 Z. L. Li, G. P. Zhang and C. K. Wang, J. Phys. Chem. C, 2011, 115, 15586-15591.
- 58 M. J. Frisch, G. W. Trucks, H. B. Schlegel, G. E. Scuseria, M. A. Robb, J. R. Cheeseman, G. Scalmani, V. Barone, G. A. Petersson, H. Nakatsuji, X. Li, M. Caricato, A. V. Marenich, J. Bloino, B. G. Janesko, R. Gomperts, B. Mennucci, H. P. Hratchian, J. V. Ortiz, A. F. Izmaylov, J. L. Sonnenberg, W. Young, F. Ding, F. Lipparini, F. Egidi, Goings, B. Peng, A. Petrone, T. Henderson, D. Ranasinghe, V. G. Zakrzewski, J. Gao, N. Rega, G. Zheng, W. Liang, M. Hada, M. Ehara, K. Toyota, R. Fukuda, J. Hasegawa, M. Ishida, T. Nakajima, Y. Honda, O. Kitao, H. Nakai, T. Vreven, K. Throssell, J. A. Montgomery Jr., J. E. Peralta, F. Ogliaro, M. J. Bearpark, J. J. Heyd, E. N. Brothers, K. N. Kudin, V. N. Staroverov, T. A. Keith, R. Kobayashi, J. Normand, K. Raghavachari, A. P. Rendell, J. C. Burant, S. S. Iyengar, J. Tomasi, M. Cossi, J. M. Millam, M. Klene, C. Adamo, R. Cammi, J. W. Ochterski, R. L. Martin, K. Morokuma, O. Farkas, J. B. Foresman and D. J. Fox, Gaussian 16, Rev. A. 03, Gaussian Inc., Wallingford, CT, 2016.
- 59 R. Liu, C. K. Wang and Z. L. Li, Sci. Rep., 2016, 6, 21946.
- 60 L. Liu, F. Sun, Y. C. Li, Y. Yan, B. X. Liu, Z. Yang, S. Qiu and Z. L. Li, Acta Phys. Sin., 2023, 72, 048504.
- 61 M. Brandbyge, J. L. Mozos, P. Ordejon, J. Taylor and K. Stokbro, Phys. Rev. B: Condens. Matter Mater. Phys., 2002, 65, 165401.

Nanoscale Paper

- 62 M. Büttiker, Y. Imry, R. Landauer and S. Pinhas, Phys. Rev. B: Condens. Matter Mater. Phys., 1985, 31, 6207-6215.
- 63 M. Walz, J. Wilhelm and F. Evers, Phys. Rev. Lett., 2014, 113, 136602.
- 64 J. Wilhelm, M. Walz and F. Evers, Phys. Rev. B: Condens. Matter Mater. Phys., 2015, 92, 014405.
- 65 M. Walz, A. Bagrets and F. Evers, J. Chem. Theory Comput., 2015, 11, 5161-5176.
- 66 Y. Q. Xue and M. A. Ratner, Phys. Rev. B: Condens. Matter Mater. Phys., 2004, 70, 081404.
- 67 G. Cabra, A. Jensen and M. Galperin, J. Chem. Phys., 2018, 148, 204103.
- 68 D. Nozaki and W. G. Schmidt, J. Comput. Chem., 2017, 38, 1685-1692.
- 69 H. Geng, X. Y. Zheng, Z. G. Shuai, L. Y. Zhu and Y. P. Yi, Adv. Mater., 2015, 27, 1443-1449.
- 70 K. Iijima, R. Sanada, D. Yoo, R. Sato, T. Kawamoto and T. Mori, ACS Appl. Mater. Interfaces, 2018, 10, 10262-10269.

- 71 M. Natali, S. Campagna and F. Scandola, Chem. Soc. Rev., 2014, 43, 4005.
- 72 L. Y. Zhu, Y. P. Yi, Y. Li, E. G. Kim, V. Coropceanu and J. L. Brédas, J. Am. Chem. Soc., 2012, 134, 2340-2347.
- 73 Y. P. Zhang, M. McDonnell, S. A. Calder and M. G. Tucker, J. Am. Chem. Soc., 2019, 141, 6310-6317.
- 74 Y. Sugo, H. Tamura and H. Ishikita, J. Phys. Chem. B, 2022, 126, 9549-9558.
- 75 M. Baghbanzadeh, C. M. Bowers, D. Rappoport, T. Żaba, L. Yuan, K. Kang, K. C. Liao, M. Gonidec, P. Rothemund, P. Cyganik, A. Aspuru-Guzik and G. M. Whitesides, J. Am. Chem. Soc., 2017, 139, 7624-7631.
- 76 M. Baghbanzadeh, C. M. Bowers, D. Rappoport, T. Żaba, M. Gonidec, M. H. Al-Sayah, P. Cyganik, A. Aspuru-Guzik and G. M. Whitesides, Angew. Chem., Int. Ed., 2015, 54, 14743-14747.
- 77 Z. Yu, Y. X. Xu, J. Q. Su, P. M. Radjenovic, Y. H. Wang, J. F. Zheng, B. Teng, Y. Shao, X. S. Zhou and J. F. Li, Angew. Chem., Int. Ed., 2021, 60, 15452-15458.